Topological wetting states of microdroplets on closed-loop structured surfaces Breakdown of the Gibbs equation at the microscale

Lin, Dongdong; Wang, Shixian; Xu, Wenwu; Chen, Yuhao; Li, Pei; Fang, Ye-Guang; Zhao, Wenhui; Duan, Xiangmei; Yang, Xinju; Jiang, Zuimin; Fang, Wei-Hai; Zeng, Xiao Cheng; Francisco, Joseph S.; Gao, Yurui

Published in:
PNAS: Proceedings of the National Academy of Sciences of the United States of America

Published: 09/04/2024

Document Version:
Final Published version, also known as Publisher's PDF, Publisher's Final version or Version of Record

Published version (DOI):
10.1073/pnas.2315730121

Publication details:
Lin, D., Wang, S., Xu, W., Chen, Y., Li, P., Fang, Y.-G., Zhao, W., Duan, X., Yang, X., Jiang, Z., Fang, W.-H., Zeng, X. C., Francisco, J. S., & Gao, Y. (2024). Topological wetting states of microdroplets on closed-loop structured surfaces: Breakdown of the Gibbs equation at the microscale. *PNAS: Proceedings of the National Academy of Sciences of the United States of America*, *121*(15), Article e2315730121. https://doi.org/10.1073/pnas.2315730121

PNAS RESEARCH ARTICLE | CHEMISTRY

Topological wetting states of microdroplets on closed-loop structured surfaces: Breakdown of the Gibbs equation at the microscale

Dongdong Lin[a,1], Shixian Wang[b,c,1], Wenwu Xu[a,1], Yuhao Chen[a], Pei Li[a], Ye-Guang Fang[b,c], Wenhui Zhao[a], Xiangmei Duan[a], Xinju Yang[d], Zuimin Jiang[d], Wei-Hai Fang[e], Xiao Cheng Zeng[f,2], Joseph S. Francisco[g,2], and Yurui Gao[b,c,2]

Contributed by Joseph S. Francisco; received September 12, 2023; accepted February 27, 2024; reviewed by Kenichiro Koga and Xuehua Zhang

Microdroplets are a class of soft matter that has been extensively employed for chemical, biochemical, and industrial applications. However, fabricating microdroplets with largely controllable contact-area shape and apparent contact angle, a key prerequisite for their applications, is still a challenge. Here, by engineering a type of surface with homocentric closed-loop microwalls/microchannels, we can achieve facile size, shape, and contact-angle tunability of microdroplets on the textured surfaces by design. More importantly, this class of surface topologies (with universal genus value = 1) allows us to reveal that the conventional Gibbs equation (widely used for assessing the edge effect on the apparent contact angle of macrodroplets) seems no longer applicable for water microdroplets or nanodroplets (evidenced by independent molecular dynamics simulations). Notably, for the flat surface with the intrinsic contact angle ~0°, we find that the critical contact angle on the microtextured counterparts (at edge angle 90°) can be as large as >130°, rather than 90° according to the Gibbs equation. Experiments show that the breakdown of the Gibbs equation occurs for microdroplets of different types of liquids including alcohol and hydrocarbon oils. Overall, the microtextured surface design and topological wetting states not only offer opportunities for diverse applications of microdroplets such as controllable chemical reactions and low-cost circuit fabrications but also provide testbeds for advancing the fundamental surface science of wetting beyond the Gibbs equation.

microdroplet | closed-loop structured surfaces | Gibbs equation | contact angle | contact shape

Significance

Controlling apparent states of microdroplets on surfaces is important for high-resolution printing and chemical reactions. Edges of textured surfaces can significantly affect the apparent shape of microdroplets. By engineering a type of microtextured surface with homocentric orthorhombic closed-loop microwalls/microchannels, facile size, shape, and apparent-contact-angle tunability of microdroplets can be achieved. Even for flat surfaces that yield completely wetting, microdroplets can entail apparent contact angles >130° on the microtextured counterparts featuring 90° edge angle. As such, the Gibbs equation widely used for accessing the apparent contact angle (typically ≤90°) of macrodroplets is no longer applicable for microdroplets and nanodroplets in the topological wetting states.

Microdroplets are often exploited for versatile applications in chemistry, material science, and industrial manufacturing (1–10), particularly in the fields of chemical engineering and biochemical microfluidics, e.g., deployed in high-efficiency microreactors and biosensing/bioscreening devices (11–17). The ultimate success of these applications requires facile production of controllable and uniform microdroplets with tunable contact-area shape and apparent contact angle. Hence, it is of great importance to acquire a microdroplet with desired shape and apparent contact angle in bio-microarrays for protein and DNA sequencing (18), liquid metal printing (19), to liquid-based fabrications (20). And particularly, in the emerging field of microdroplet reaction, the chemical reactions are largely dependent on the size and the surface of the microdroplets (21–25). Realizing microdroplet control with high accuracy and high dimensions (shape, size, and contact angle) would be crucial to precisely controlling the printing/coating patterns and chemical reactions.

Adjusting the surface chemistry and textures has been widely employed for controlling the morphology of the contacting droplets and the wettability of the contact surface. Two prototypical wetting states for the microdroplets are well known as Wenzel and Cassie–Baxter states. In the former, the droplet fully contacts a rough surface, whereas in the latter, the droplet contacts only the apex area of the rough surface, with air pockets trapped between it and the "valley" portion. Quantitative characterizations of the two wetting/dewetting states were given by the Wenzel (26) and Cassie (27) relationships, respectively. Consequently, increasing roughness on hydrophilic surfaces improves wettability. Additionally, high roughness can result in enhanced capillarity and contact line pinning effects, leading to intriguing properties of the Wenzel droplet, including unidirectional liquid spreading and formation of polygonal thin liquid films or droplets (28–31). For instance, Courbin et al. (28) found that liquids deposited on microtextured surfaces can form square-, hexagonal-, octagonal-, and circular-shaped thin-liquid films. Raj et al. (29) reported an approach to tailor various shapes of the droplet contact area, ranging from squares, rectangles, hexagons, and octagons to dodecagons, by designing either structural or chemical heterogeneities on the surface. While these strategies employing micropillared

Reviewers: K.K., Department of Chemistry, Okayama University; and X.Z., Department of Chemical and Materials Engineering, University of Alberta.

The authors declare no competing interest.

[1]D.L., S.W., and W.X. contributed equally to this work.

[2]To whom correspondence may be addressed. Email: xzeng26@cityu.edu.hk, frjoseph@sas.upenn.edu, or gaoyr@nanoctr.cn.

This article contains supporting information online at https://www.pnas.org/lookup/suppl/doi:10.1073/pnas.2315730121/-/DCSupplemental.

Published April 1, 2024.

surfaces demonstrated success in controlling droplet morphology, it is crucial to recognize that these surfaces inherently impose limitations on the range of passively attainable shapes. Furthermore, the contact angle (CA) on such surfaces depends on the wetting state. In cases where the droplet adopts a Wenzel state, the CA consistently remains smaller than the intrinsic CA of the surface material. This inherent limitation restricts the controllability of CA, particularly in scenarios involving completely wetting liquid/material combinations (i.e., Young's contact angle $\theta_Y \sim 0°$). Therefore, given the detailed liquid/material combinations especially for superhydrophilic surfaces, it is important to develop an approach for precise control of both droplet shape and CA (θ_A) over a wide range. This is particularly important for those applications demanding precise control and high spatial resolution, despite previous reports of achieving $\theta_A > \theta_Y$ on certain hydrophilic surfaces (28, 32).

It is known that solid edges are ubiquitous on textured surfaces and play an important role in dictating the wetting behavior of microdroplets (29, 30, 33–36). The three-phase contact line (TCL) pinned at the pillar edges of structured surfaces, for example, introduced an energy barrier for the liquid propagation, thereby offering a control of θ_A of microdroplets (29, 37). To retrospect the edge effect, it is essential to examine the typical scenario where a droplet is placed atop a single pedestal or pillar. In this context, if the droplet is small with TCL away from the edge, the droplet takes its equilibrium/intrinsic θ_Y. Otherwise, if the droplet becomes larger with the TCL reaching the edge, the edge hinders the droplet from further spreading, even if θ_A would exceed the θ_Y value. The critical contact angle θ_c, beyond which the liquid will spill over the sides of the pillar, was given by the Gibbs equation (37),

$$\theta_c = \theta_Y + (180° - \phi), \qquad [1]$$

where ϕ is the edge angle, i.e., the angle subtended at the intersection of the two solid surfaces forming the edge. A derivation from the original Gibbs inequality to Eq. **1** is given in *SI Appendix*, section 1. Notably, if $\phi = 90°$, then $\theta_c = \theta_Y + 90°$.

Much efforts have been devoted to studying the edge effect on wetting. For instance, Oliver et al. (38) experimentally examined Eq. **1** by investigating the spreading behavior of water droplets on pedestals with a wide range of edge angles. They concluded that Eq. **1** was mainly a purely geometrical consequence, hardly dependent on the intrinsic wettability of the edge. Bayramli et al. (39) further confirmed experimentally the applicability of Eq. **1** for edges with $\theta_Y = 0°$. Although Dyson (40) later commented on the limited application conditions of Gibbs inequalities, the inequalities he proposed had already been attributed to the Gibbs theory by Oliver et al. (38). To date, Eq. **1** has been widely employed to explain droplet wetting phenomena taking place on micro/nano-structured surfaces (29, 34–36).

The incorporation of concentric and closed-loop microwalls/microchannels on a surface can take full advantage of the edge effects, introducing strong pinning for both Cassie and Wenzel states, while having robust control over droplets (41). In this work, we designed surfaces with closed-loop microstructures with varied shapes and well-controlled orthorhombic edges. This design allowed us to control both the contact-area shape and apparent CA of droplets over a wide range. Our work is remotely related to two previous studies (41, 42). Debuisson et al. fabricated concentric circle micropatterns of defects/channels using photoresist SU-8, displaying smooth edge angles that were intricate to identify, and developed a 2D model predicting the CA hysteresis. Liimatainen et al. fabricated chemically heterogenous closed-loop circular and square patterns with undercut sharp edges, akin to a "T" or an umbrella, utilizing a silicon background with a silicon oxide top layer. Their investigation demonstrated controllable spreading and anisotropic wetting of liquids on these surfaces. However, in both previous studies, completely wetting liquid/material combinations and precise edge-angle control were not considered. Hence, edge angle correlation with the CA was not reported.

As a comprehensive study, here, we fabricated surfaces composed exclusively of a single pure material of silicon, featuring closed-loop micropatterns in diverse patterns, including not only regular shapes such as circle, triangle, square, rectangle, pentagon, hexagon, and octagon but also intricate patterns like heart shape. Moreover, we extended droplet control to considerably broader array of morphologies, and even to irregular shapes tailored to meet possible specific requirements. Together with the shape control, we further considered the dimension of CA control at the same time and proposed to manipulate CA across a broad range, particularly for intrinsically completely wetting liquid/material combinations, by bringing together the droplet evaporation and the close-loop geometry. This exploration facilitated precise and high-dimensional control over droplets. Of particular significance was that we were able to conduct a comparative analysis of the droplet's CA with the edge angle, as we intentionally and precisely controlled the edge angle. Through this examination, we revealed the surprising deviation of the measured CA from the prediction of Gibbs equation (1). The deviation appeared to be a generic behavior, not only seen for water but also for other liquid droplets, such as alcohols and hydrocarbon oils. Especially, when $\theta_Y \sim 0°$, the critical CA could be as large as >130°, with an extra increase of >40° compared with the known Gibbs equation–derived 90°. We attributed the large deviation to the water–surface interaction and atomic structure of the edge and suggested adding a correction term in the Gibbs equation to account for the apparent deviation.

Results and Discussion

We applied lithography technology to fabricate a variety of microtextured silicon (Si) surfaces with closed-loop orthogonal microwalls/microchannels (detailed in *Materials and Methods*). Fig. 1*A* shows top view of a micropatterned surface consisting of 15 concentric circular microwalls/microchannels (*SI Appendix*, Fig. S2). The edge angles were well controlled around 90°, showing negligible deviations (*SI Appendix*, Fig. S3). The width of the microwalls and microchannels and the height of the microwalls are denoted as W_w, W_c, and H, respectively. The intrinsic contact angle θ_Y value of the surface, i.e., CA of the corresponding flat counterpart, was modified via a 10 min UV/ozone treatment, which led to $\theta_Y < 3°$ for water microdroplets (see *Left* panel of Fig. 1*C*). Here, as the intrinsic contact angle is so small, experimentally, it is difficult to distinguish its difference with the exact 0° angle. Hence, it is not unreasonable to view $\theta_Y \sim 0°$. Additionally, the stability of the intrinsic superhydrophilicity of the flat counterpart was examined. *SI Appendix*, Fig. S4 demonstrates water microdroplets deposited on a flat Si surface at different times after UV/ozone treatment, showing that θ_Y exhibited little change within 1 h. Even up to 25 h, θ_Y increased only slightly to ~8°. It should be noted that all our experimental tests, including contact angle measurements, were immediately performed once the UV/ozone treatment finished. Most tests were completed within 30 min. Therefore, during all our experiments in which UV/ozone treatment were undertaken, the intrinsic contact angle θ_Y remained ~0°.

Sub-micro water droplets were then immediately deposited onto the UV/ozone-treated micropatterned surfaces using a home-made injection micropump. As θ_Y remained ~0° during our

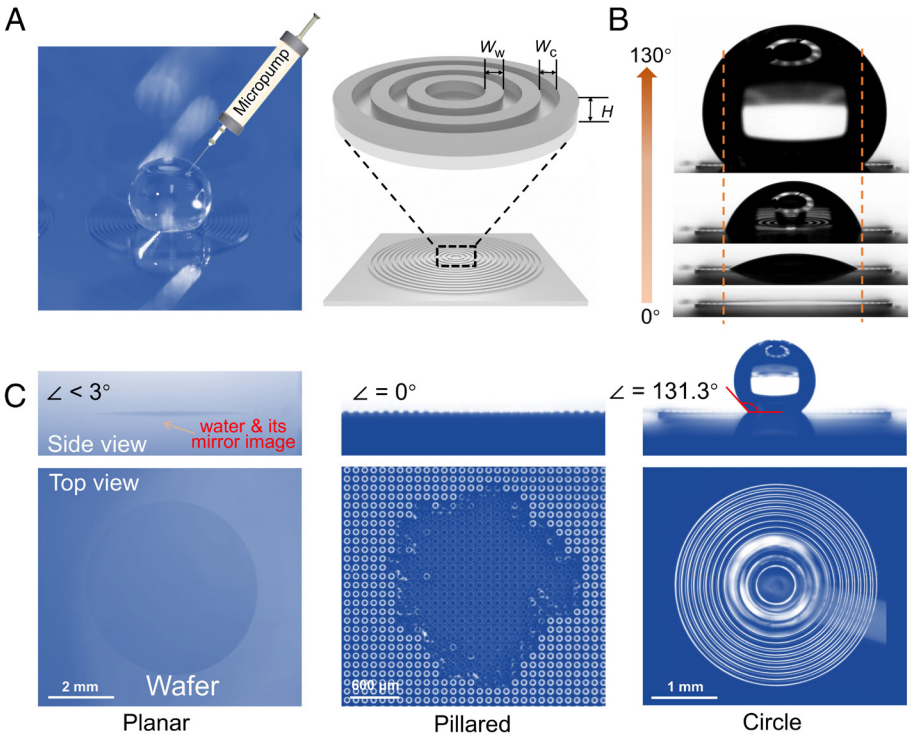

Fig. 1. Droplets with apparent contact angles (CAs) tunable over a wide range. (*A*) Microlens photograph of a representative Wenzel state of a water microdroplet (*Left*) located on a fabricated surface consisting of circular microwalls/microchannels (*Right*) and having a superhydrophilic chemical composition. The droplet was produced using an injection micropump (see schematic illustration). The widths of the microwalls and microchannels are denoted as W_W and W_C, respectively, and the height of the microwalls is denoted as H. (*B*) Side views of water droplets on the fabricated surface, exhibiting CA values ranging from 0° to 130°. (*C*) Side and top views of water droplets on the 10 min UV/ozone-treated planar wafer (*Left*), micropillared surface (*Middle*), and surface with circular closed loops ($W_W/W_C/H$ = 50/50/60 μm, *Right*). On a planar wafer, the measured Young's contact angle (θ_Y) of the water droplet was <3°, approximating 0°. On the surface with micropillars, the water droplet exhibited a CA of 0° (completely wetting state), consistent with the Wenzel relationship. In contrast, on the surface with circular closed loops, the maximum CAs of the water droplet were ~131°.

experiments, the location of the TCL of the droplet remained pinned at the outer edge of the microwalls (either during deposition or evaporation, Movie S1). This behavior is consistent with our previous simulational report (5). Interestingly, the stable droplet showed multiple Wenzel states, with TCL depending on the location of the microwalls; θ_A varied over a wide range, from 0° to ~130° (Fig. 1*B*). This wide range of θ_A values, from complete wetting to strong dewetting states, is surprising for surfaces involving pinning effects with $\theta_Y \sim 0°$ (17, 26–28), hence representing a significant advancement in realization of multiple metastable Wenzel states.

To better understand the observed multiple metastable Wenzel state, we fabricated a topological non-closed-loop surface, i.e., a micropillared Si surface consisting of square arrays of circular pillars with heights of 60 μm, diameters of 50 μm, and interpillar spacings of 50 μm (*SI Appendix*, Fig. S2*E*). Water exhibited complete wetting, i.e., $\theta_A = 0°$, regardless of the final droplet size (see *Middle* panel of Fig. 1*C* and Movie S2), consistent with the Wenzel relationship. In contrast, on a surface with closed-loop microwalls/microchannels ($W_w = W_c = 50$ μm, $H = 60$ μm), water exhibited much larger θ_A values, even reaching 131.3° (see *Right* panel of Fig. 1*C*). These results indicate that the closed-loop topology of the surface texture is responsible for the observed multi-Wenzel states with θ_A being over a wide range, hence named as the topological wetting states.

The importance of the closed-loop topology was further confirmed by examining the dynamic wetting behavior of water droplets on a slightly modified surface with circular microwalls, in which we artificially created a small microhole (width ~50 μm) on each of the sixth to outermost 15th microwalls (*SI Appendix*, Fig. S5*A*). This specially designed surface involved a closed-loop topology in the inner region, but a non-closed-loop topology in the outer region. On this surface, smaller water droplets exhibited the topological wetting states so long as their TCL was pinned within the inner five closed loops; on the other hand, larger droplets collapsed when the TCL crossed the fifth closed loop and reached the sixth loop with a microhole (*SI Appendix*, Fig. S5*B* and Movie S3). Although these microholes can be viewed as small perturbations in terms of changing the overall roughness ratio r (Wenzel equation), they actually changed the topology (or genus value, a topological invariant in mathematics for describing the number of "holes" or "handles" of the microstructures/microchannels) from closed-loop to non-closed-loop for the outer region of the surface. Therefore, this region allowed the water droplet to leak through the microholes and eventually reach the flat region beyond the outermost 15th loop, suppressing the topological wetting states that would exist if the 6 to 15th loops were closed. Considering the closed-loop topology remained the largest edge effect all along the TCL, the beading-up microdroplet needed edge everywhere on the TCL.

In view of the high tunability of the droplet TCL on surfaces with closed-loop microwalls/microchannels and the high interest in droplet control, we further examined the feasibility of controlling the contact angle, contact-area shape, and size of the microdroplets by designing the closed-loop roughness in the following. First, the apparent CA and spreading behavior of a growing microdroplet were first demonstrated. Sub-micro water droplets were gradually injected onto the surfaces with circular closed loops immediately after UV/ozone treatment (Movie S4). As the number of injections increased, the droplet became larger while the TCL moved outward

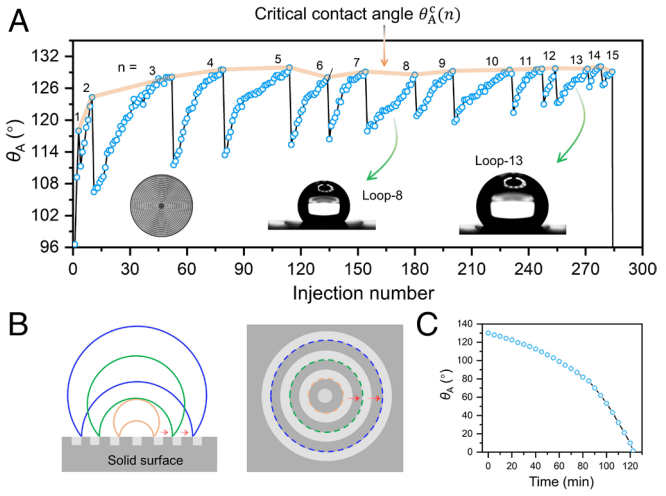

Fig. 2. CA and spreading behavior of a growing droplet and evaporation of the droplet on UV/Ozone-treated rough surface with circular closed-loop microwalls/microchannels (θ_Y ~ 0°). (*A*) Measured CA values of water droplet vs. sub-microdroplet titrimetric/injection number. In general, θ_A increases with increasing number of sub-microdroplets. Within each loop *n*, the water droplet is in the loop-*n* Wenzel state and the maximum θ_A corresponds to the critical contact angle $\theta_A^c(n)$. Once θ_A exceeds $\theta_A^c(n)$, the water droplet transforms into the next loop-(*n*+1) Wenzel state. (*B*) Schematic illustration of the CA change and TCL hop during the droplet growing process. The orange, green, and blue solid lines represent the lower or upper profile of the microdroplet during the growing process, while orange, green, and blue dash lines represent the TCL location of the microdroplet, which is pinned at the outer profile of the microwall of the corresponding loop, and hop to the next dash line during transition from one topological wetting state to the next. (*C*) CA values of loop-*n* Wenzel state vs. time during droplet evaporation at 24 °C.

stepwise, from the first (inner) to the fifteenth (outermost) loop (Fig. 2 *A* and *B* and *SI Appendix*, Fig. S6). For ease of discussion, hereafter the Wenzel state with TCL pinned at the *n*th closed-loop microwall is named loop-*n* Wenzel state. The evolution of θ_A for the growing water droplet is shown in Fig. 2*A*. In each loop-*n* Wenzel state, θ_A increased with the volume of the water droplet, while the TCL was pinned at the outer edge of the corresponding (*n*th) microwall due to the enduring θ_Y ~ 0° of the surfaces. The trend of increasing θ_A in each closed-loop can be well explained by the pinning mode of the droplet (*SI Appendix*, section 7). When the water droplet reached a critical size, i.e., when θ_A reached a critical value, a transition occurred from the loop-*n* to the loop-(*n*+1) Wenzel state, while the TCL moved outward to the (*n*+1)-th microwall. The corresponding θ_A value is called critical contact angle $\theta_A^c(n)$ of the loop-*n* Wenzel state, corresponding to the maximum CA value for the loop (Fig. 2*A*). The $\theta_A^c(n)$ values for different loops were nearly the same, ~130° in this case. Additionally, our deduction showed that the minima of $\theta_A(n)$, denoted as $\theta_{min}(n)$, increased with increasing the radius of concentric closed-loop microwalls, well explaining the observed shallower $\theta_{min}(n)$ for larger droplets in Fig. 2*A* (see *SI Appendix*, section 7 for the detailed deduction).

After the formation of the loop-*n* state with θ_A ~ 130°, we monitored the evaporation of the droplet at room temperature (24 °C, Movie S5). Remarkably, the TCL remained at the *n*th microwall while θ_A decreased gradually to 0° (Fig. 2*C*). Due to the slow rate of evaporation, the droplet can be considered in equilibrium state. Additionally, the contact angle, including the critical CA remained nearly constant for an extended period before a considerable evaporation at room temperature, indicative of the stability of the topological wetting state. Naturally, if the evaporation was purposely stopped at a certain time, a metastable droplet with the desired θ_A can be obtained. Therefore, the contact area (or size) and θ_A value of the droplet can be precisely controlled via either the stepwise precise liquid injection or truncating the evaporation of the droplet with a desired θ_A.

The contact-area shape of the droplet can also be controlled, by engineering a surface with a predesigned microwall shape. As shown in Fig. 3, the contact area of the droplet could be tailored into circle, triangle, square, rectangle, pentagon, hexagon, octagon, dodecagon, and even irregular heart shapes, essentially matching the shape of the microwalls. Besides the shapes displayed here, we expect that droplets with other irregular shapes could be easily achieved with tunable θ_A values by predesigning closed-loop structured surfaces. The three-dimensional (3D) shape of the droplet can thus be highly anisotropic (*SI Appendix*, Fig. S7 and Movies S6–S8). As an example, *SI Appendix*, Fig. S7*C* shows the strong anisotropy of a droplet shape on the surface with triangular closed loops. The largest θ_A was seen at the side of the triangle, while the smallest θ_A was observed at the vertex. Consistent with the shape of the microwalls, the droplet exhibited threefold rotational symmetry. Additionally, a finite-element method (43) was also employed to investigate the equilibrium shape of droplets, which demonstrated consistent morphologies and anisotropic CA (see *SI Appendix*, section 8 and Fig. S9 for details). Interestingly, the maximum $\theta_A^c(n)$ values on the circular, triangular, square, and rectangular closed-loop surfaces were all approximately 130° (Figs. 2*A* and 4 *A*–*C*), regardless of the size and shape of the loops. This indicates that all closed-loop microwalls (with the same structural parameters) involved nearly the same strongest pinning interactions, reflecting their topological invariability.

Notably, in the above experiments, regardless of the geometry of the closed-loop microwalls on the surfaces, the critical CA of the microdroplets should be 90° according to Gibbs equation (1) if θ_Y ~ 0° and edge angle ϕ ~ 90°. However, in the topological wetting states, the largest CA was ~130°, ~40° larger than that predicted based on the Gibbs equation. Before further discussion, we first experimentally confirmed the conventional situation where a millimeter droplet was placed on a surface with macrotexture, i.e., a single cylindrical platform (quartz, radius 2.5 mm, height 1 mm). Water and ethanol millimeter droplets showed θ_Y = 39.2° and 7.6°, respectively. And the corresponding critical CAs at the edge were measured to be 131.5° and 95.2°, respectively, (Fig. 5), both very close to the values (129.2° and 97.6°)

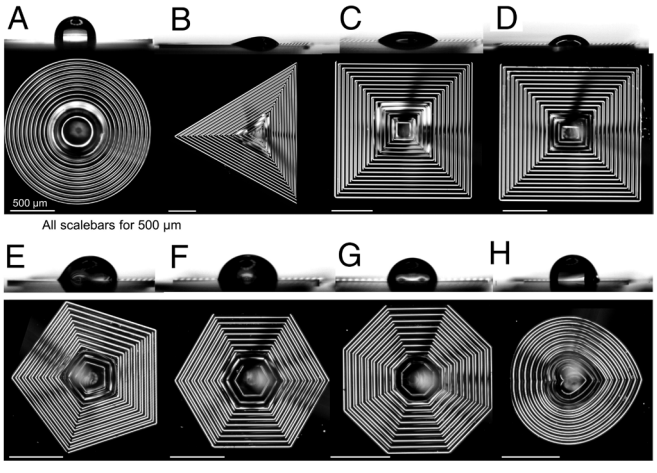

Fig. 3. Highly tunable droplet shapes on UV/Ozone-treated rough surface with closed-loop microwalls/microchannels (θ_Y ~ 0°). Side and top views of water droplets on surfaces with closed-loop microwalls/microchannels in different shapes ranging from (*A*) circle, (*B*) triangle, (*C*) square, (*D*) rectangle, (*E*) pentagon, (*F*) hexagon, (*G*) octagon, to (*H*) heart shapes. Droplets in smaller contact angles were chosen here to show the contact shape.

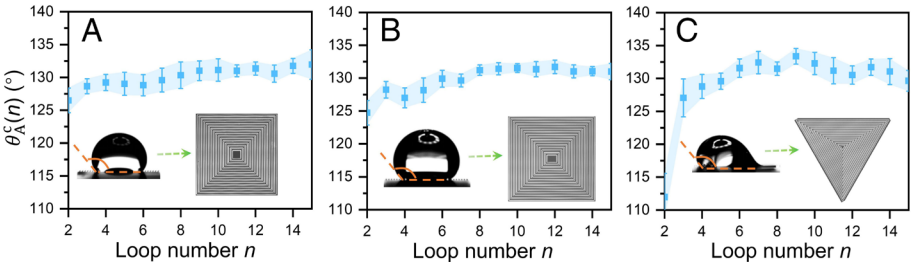

Fig. 4. Measured θ_A^c (n) vs. loop number n for droplet on UV/Ozone-treated rough surfaces with (*A*) square-, (*B*) rectangle-, and (*C*) triangle-shaped closed-loop microwalls/microchannels. The θ_A^c (n) values were measured along the line-of-sight (denoted by green dashed arrows toward the *Right Inset*) at the (shorter) sides of the squares, rectangles, and triangles. The light-blue color denotes SD error bands.

from the Gibbs equation, with the deviations within 2.4°. This independent experiment confirms the Gibbs equation for millimeter droplets at conventional edges.

On the other hand, our previous simulation work had demonstrated that for a nanodroplet on surfaces (θ_Y = 0° on the flat surfaces) with closed-loop nanowalls/nanochannels, its critical CA changes between 70° and 50°, largely deviating from 90°. Hence, it appears that the conventional Gibbs equation is not applicable for nanodroplets on nanotextured surfaces with closed-loop nanowalls/nanochannels. To further confirm this conclusion, we performed larger-scale MD simulations using a nanodroplet on a platform with a height of 48 Å and an edge angle of 90°. The critical CA for the edge with different representative surface-water interactions was shown in Table 1 and *SI Appendix*, Fig. S10. Clearly, for θ_Y = 0°, the surface-water interaction could be different, leading to different critical CA ranging from 0° to 102.9°, rather than being universally 90°. As for the cases of θ_Y = 29.7° and 55.4°, the obtained critical CAs from MD simulations were 115.4° and 132.7°, respectively, being 85.7° and 77.3° (rather than being 90° or 180°—ϕ) larger than the corresponding θ_Y. All these simulations indicated the breakdown of the Gibbs equation for nanodroplets on nanotextured surfaces.

The observed deviation of θ_c is likely due to the combined effects of water–surface interaction and atomic structures of the edge. The former had been confirmed by the large deviation of critical CA values at θ_Y = 0° in Table 1. For the latter, we constructed a new edge based on FCC (111) surface, showing an edge angle of 90° in the nanoscale. However, when θ_Y = 0° (water–surface interaction parameter ε_{sw} = 0.018 eV) and 56.3° (ε_{sw} = 0.015 eV), the critical CA is 121.9° and 141.3°, respectively (*SI Appendix*, Fig. S11), markedly different from the values (0° to 102.9° and 132.7°, respectively) at similar θ_Y (namely θ_Y = 0° and 55.4° shown in Table 1 and *SI Appendix*, Fig. S10) on the edge composed of simple cubic (100) structure. This indicates the important role of atomic structures of the edge on the critical CAs. We noticed that although the deviation on the micropatterned (experimental) and the nanopatterned (simulational) surfaces seemed different, due to the different scales and atomic structures, they all suggested the breakdown of the Gibbs equation.

Note that with macroscale surface texture and the conventional edge, the apparent contact angle of macrodroplets seems insensitive to the combined effects of the water–surface interactions and the atomic structures which are much more important at a much smaller scale. Moreover, the macroscale edge is not sharp if viewed from the microscopic scale (containing atomic steps and possible defects), giving an averaging outcome of varying curvature. Why this varying curvature yields an approximate 90° edge angle requires more in-depth and systematic studies in the future. To quantitatively describe the deviation from the Gibbs equation, we introduce a correction term, θ_{ex}, given by Eq. **2**:

$$\theta_c = \theta_Y + (180° - \phi) + \theta_{ex}. \quad [2]$$

To measure θ_{ex} for microdroplet on closed-loop surfaces with different intrinsic wettability, we employed the fabricated closed-loop Si surfaces without UV/ozone treatment and varied θ_Y by depositing different types of liquids. On the untreated surface, the water droplet had an intrinsic θ_Y of 62.6° (*SI Appendix*, Fig. S12), while other lower-surface-tension liquids show 0° value for θ_Y. In particular, three completely wetting liquids i) isopropanol (C_3H_8O), ii) ethanol (C_2H_5OH), and iii) decane ($C_{10}H_{22}$), all showed θ_Y = 0°, while another Si-superphilic liquid octane (C_8H_{18})

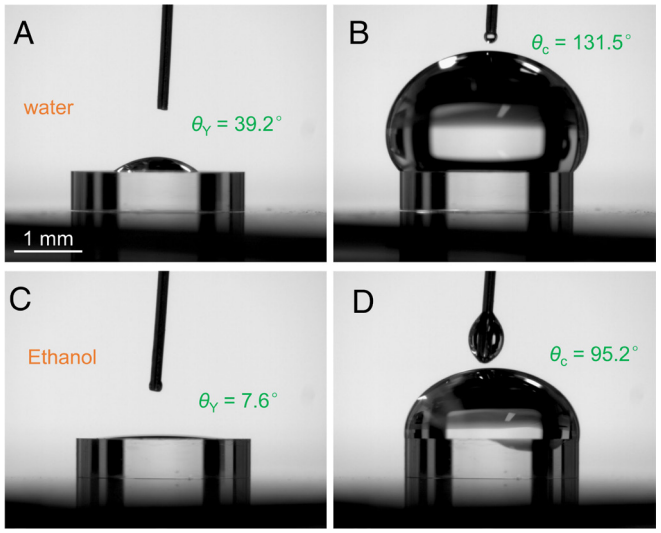

Fig. 5. Re-examination of the Gibbs equation on a conventional millimeter quartz platform (cylindrical, radius 2.5 mm, height 1 mm, ϕ = 90°). A millimeter water droplet with TCL (*A*) far from the edge (θ_Y = 39.2°) and (*B*) at the edge with the critical contact angle (θ_c = 131.5°); A millimeter ethanol droplet with TCL (*C*) far from the edge (θ_Y = 7.6°) and (*D*) at the edge with the critical contact angle (θ_c = 95.2°).

Table 1. Critical CA of the water nanodroplet on an atomic edge (height 48 Å; edge angle ϕ = 90°)

ε_{sw} (eV)	θ_Y (°)	θ_c (°)	SD (°)
0.031	55.4	132.9	0.4
0.036	29.7	115.4	0.1
0.038	0	102.9	0.2
0.040	0	95.0	0.1
0.041	0	89.7	0.1
0.043	0	74.6	0.1
0.045	0	52.2	0.3
0.047	0	32.4	0.3
0.050	0	0	0

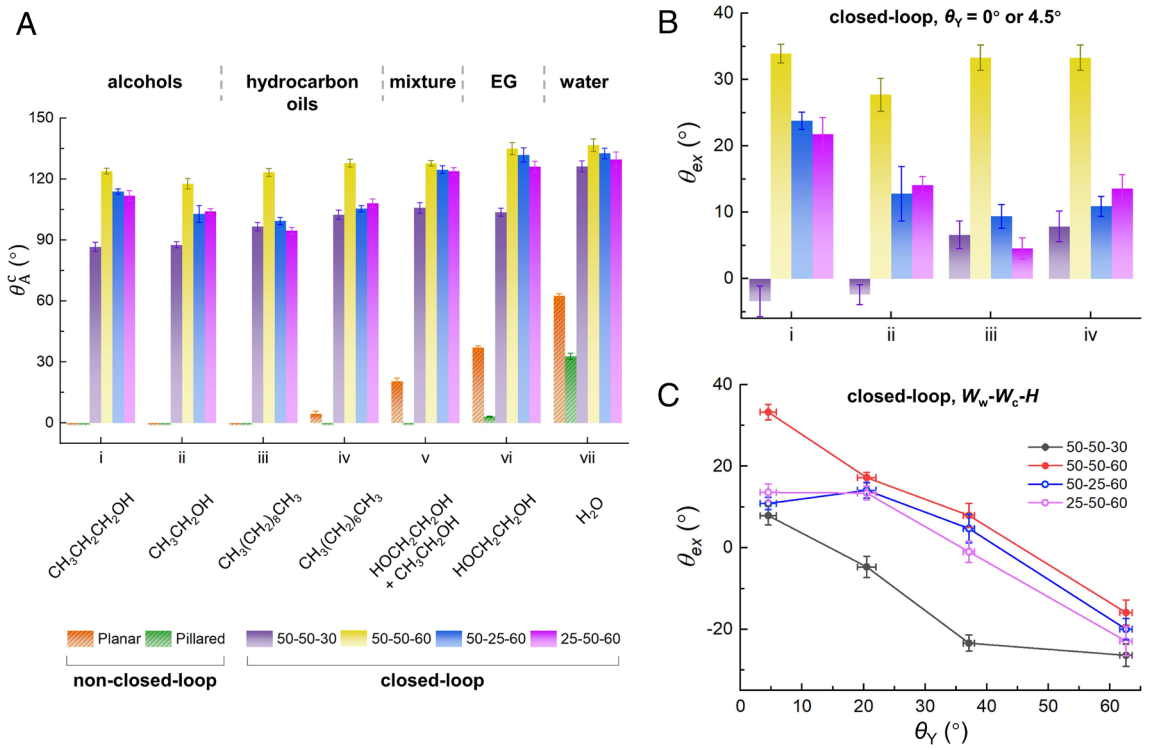

Fig. 6. Deviations of critical CAs on UV/Ozone-untreated surfaces. (*A*) Critial CAs θ_A^c of seven liquids [i–vii] on planar, micropillared, and closed-loop surfaces with different $W_w/W_c/H$ values. The numerical values in the legends, such as 50-50-30, subsequently represent the dimensional length of W_W, W_C, and H (in the unit μm). All surfaces are UV/Ozone-untreated. All liquids exhibit a much larger tunability on surfaces with the closed-loop microtextures than on surfaces without the closed-loop microtextures. It should be noted that when the angle value is 0°, we reset it to −1° in (*A*) to display the bar. (*B*) θ_A^c deviations (θ_{ex}) of super-Si-philic liquids [i-iv], and (*C*) θ_{ex} as a function of θ_Y, on the four closed-loop surfaces. SD error bars were used based on three measurements.

showed θ_Y = 4.5°. All liquids exhibited θ_A = 0° on untreated nanopillared surfaces (Fig. 6 *A* and *B*). In contrast, as they were deposited onto the closed-loop surfaces (four surfaces employed with closed-loop parameters $W_w/W_c/H$ = 50/50/30, 50/25/60, 25/50/60, and 50/50/60 μm, *SI Appendix*, Fig. S13), they exhibited critical CA ≫ 0°, mostly >90°, at the topological wetting states. Especially for H = 60 μm, the critical CA can be even as large as 127.8°. It is notable that a larger W_w or W_c or H value results in a larger critical contact angle, consistent with our previous simulation (5). Therefore, the microtextured surface with $W_w/W_c/H$ = 50/50/60 μm always displayed the largest θ_c value. Next, on the four UV/ozone untreated surfaces, liquids with a gradually increasing θ_Y from 4.5° to 62.6° were deposited. The dependence of θ_{ex} on θ_Y was shown in Fig. 6*C*, indicating a general trend of decreasing θ_{ex} with increasing θ_Y. In other words, smaller θ_Y leads to larger θ_{ex}, while too large θ_Y could even yield negative θ_{ex}. Nevertheless, the closed-loop surfaces result in high tunability toward different types of liquids, regardless of the liquid–surface interaction. However, the critical contact angle tends to approach 90°, i.e., the value predicted by the Gibbs equation, (see *SI Appendix*, section 11 for more details) when the microwalls becomes certain high.

Conclusion

In conclusion, we experimentally observed multiple topological wetting states characterized by large apparent contact angles of microdroplets on microtextured surfaces with a series of homocentric and closed-loop microwalls/microchannels. These topological wetting states fundamentally correlate the surface wetting with the surface topology. Inspired by this, a generic strategy was proposed to achieve precise control of microdroplets with arbitrary contact-area shapes and θ_A over a wide range, by engineering closed-loop structured surfaces. Even for the intrinsically superhydrophilic surfaces (θ_Y ~ 0°), θ_A can be tailored over a wide range between 0° and >130°, indicating that the underlying closed-loop surfaces become strongly hydrophobic. Meanwhile, the shape and size of the droplets can be controlled by designing the shape and size of the closed-loop microstructures, for example, in the form of circle, triangle, square, pentagon, hexagon, octagon, dodecagon, and heart shape, and other irregular shapes, with predefined sizes. On these surfaces, importantly, the critical contact angle no longer satisfies the Gibbs equation, a conclusion applicable to various liquids including water, alcohols, and hydrocarbon oils. Especially, for intrinsically superhydrophilic surfaces with θ_Y ~ 0°, the critical contact angle could be as large as >130°, with an extra increase of >40° compared to the generical value of 90° based on the Gibbs equation. The deviation from 90° was attributed to combined effects of the water–surface interactions and atomic structures at the edge. These findings may have important implications to controllable microdroplets in microfluidic, chemical reactions and biosensing applications.

Materials and Methods

Fabrication of Micropatterns on Si Surfaces. The microfabrication (*SI Appendix*, Fig. S14) of the designed patterns started with an N-doped silicon wafer (10 Ω) with 4-inch diameter. The AZ P4620 (MicroResist) photoresist was spin-coated on the wafer at the rate of 4,000 rpm for 30 s. The photoresist thickness was measured to be ~6.8 μm by a step profiler. Following soft baking for 90 s at 95 °C, the wafer was lithographically exposed to UV light with a contact mask aligner (Karl Suss MA6, Germany) for micropattern definition. The exposure energy was 9 mW/cm^2. Tetramethylammonium hydroxide (TMAH, 1:8) was applied for development at 25 °C. Deep ion reaction etching (DIRE, STS HRM) was used to etch 60 μm deep

micropatterns on Si, where SF_6 and C_4F_8 were employed for etching and passivation layer deposition, respectively. The etching time for one cycle was set to 6 s, including 2 s passivation (150 sccm) and 4 s etching (200 sccm). The etching speed was set at ~6 μm/min. Then, the resist layer was removed by acetone and ethanol, and the wafer was cleaned in HF solution (2%). In addition, oxygen plasma etching was applied to fully remove the residual photoresist. Finally, the wafer was diced and rinsed with deionized (DI) water.

UV/ozone treatment (CIF International Group Co., Ltd.) was applied to tune the intrinsic wettability of the Si surfaces. Before the treatment, the substrates were washed with acetone, ethanol and water, respectively. The UV irradiation power density was 30 $\mu W/cm^2$. The wettability of the Si surfaces after UV/ozone treatment was dependent on the exposure time. After 10 min of treatment, the Young's contact angle of the water droplet was <3°.

Surface Characterization. A SU-70 field-emission microscope (Hitachi) with an accelerating voltage of 5 kV was used to examine the surface morphology. Elemental compositions were analyzed by energy-dispersive spectrometry (EDS, AMetek EDAX, Apollo X). To measure the larger-scale structures of the designed micropatterns, we used a tabletop scanning electron microscope (TM3000, Hitachi) with an accelerating voltage of 15 kV. A step profiler (Bruker, Dektak XT) was used to measure the height of the fabricated structures. The optical microscopy and SEM images indicated the successful preparation of concentric microstructures on Si wafers with smooth internal edges (*SI Appendix*, Fig. S2 *A* and *B*), without notable defects and damages. The EDS analysis revealed that only a single chemical component (Si) was present in the fabricated structures (*SI Appendix*, Fig. S2 *B* and *C*).

The UV/ozone-treated surfaces were characterized by atomic force microscopy (AFM, Multimode VIII, Bruker Nano Surface, USA) in tapping mode with a gold-coated Si tip (scanning rate 1 Hz, resolution 256 lines) at room temperature and low humidity (35%).

Evaporation Experiments. The evaporation was performed naturally at room temperature (24 °C) with a humidity of 30 ± 5%.

Contact Angle Measurements. The contact angles of droplets on the as-prepared substrates were measured with a standard contact angle goniometer (KRÜSS, DSA25), equipped with customized multicameras in different directions, including horizontal, vertical, and different oblique directions. A high-speed camera capable of capturing 1,000 frames per second was applied to record the evolution of droplets. Seven different types of liquids [DI water, C_2H_5OH, $(CH_2OH)_2$, $(CH_2OH)_2$/C_2H_5OH mixture (1:1), C_3H_8O, and two hydrocarbon oils, C_8H_{18} and $C_{10}H_{22}$] were deposited separately, either using an automatic microinjector or by hand with a screw microinjector, at room temperature and 60% relative humidity. In order to produce a small-volume droplet, a bent needle with a diameter of either 60 or 110 μm was equipped on the injector, enabling the injection of sub-microdroplets of 0.03 to 0.1 μL onto the surface. All measurements were conducted in a vibration isolator. Moreover, the evaporation experiment was performed at room temperature. The droplet was captured and the CA was measured every 5 min.

Measure of Intrinsic and Critical CAs on Conventional Millimeter Quartz Platform. A cylindrical quartz platform (radius 2.5 mm, height 1 mm) was cleaned with ethanol and deionized water and finally dried with gentle flow nitrogen gas. Then, the cylinder was placed on a horizontally calibrated contact angle test platform. Water or ethanol droplet in millimeter was deposited on the platform by the stepwise sub-microinjection, with TCL far away from or reaching at the edge, where the intrinsic CA and the critical CA were measured respectively.

Molecular Dynamics Simulations. MD simulations were performed using the Large-scale Molecular Massively Parallel Simulator (LAMMPS) package (44). Water molecules were described by the coarse-grained monatomic water (mW) model (45). The surface atoms interacted with each water molecule via the 12–6 Lennard–Jones (LJ) potential with LJ parameter $\sigma_{sw} = 3.2$ Å, whereas LJ parameter ε_{sw} can be varied. The van der Waals cutoff was set to 10.0 Å. The rough surfaces were constructed with two layers of surface atoms as the bottom substrate, above which were the platform composed of layers of atoms in the normal (z) direction. Two series of MD simulations were performed with different structured model surfaces [simple cubic (100) surface and FCC (111) surface structures]. The lattice constant of both structures was 4 Å. A slab-like simulation box, relatively thin in the y direction [40 Å for simple cubic structure and 42.4 Å for FCC (111) surface] and relatively long in the x direction [188 Å for simple cubic structure and 196 Å for FCC (111) surface] and z direction (400 Å), was adopted. Periodic boundary conditions were applied in all three dimensions, thus the water slab was infinite in the y direction. For simplicity, all the surface atoms were fixed throughout the MD simulations. Newton's equations of motion were integrated using the velocity Verlet algorithm with a time step of 5 fs. MD simulations were performed in the *NVT* ensemble, with the temperature maintained at 300 K using the Nosé–Hoover thermostat. The simulation time of each system was >40 ns.

Data, Materials, and Software Availability. All study data are included in the article and/or supporting information.

ACKNOWLEDGMENTS. We thank Prof. Y. Zhao, Prof. T. Cui, and Dr. F. Zhao for discussions and Prof. L. Wang and Dr. B. Wang for giving great help in sample fabrications. Y.G. was supported by the National Natural Science Foundation of China (NSFC, No. 22273014) and the National Key Research and Development Program of China (No. 2022YFA1203200). D.L. was supported by the NSFC (No. 11804174), the Qian Xuesen Collaborative Research Center of Astrochemistry and Space Life Sciences Fund and the K. C. Wong Magna Fund from Ningbo University. X.C.Z. acknowledges the support of the Hong Kong Global STEM Professorship Scheme and by the GRF grant (11204123) of the Research Grants Council of Hong Kong.

Author affiliations: [a]Department of Microelectronic Science and Engineering, School of Physical Science and Technology, Ningbo University, Ningbo 315211, China; [b]Laboratory of Theoretical and Computational Nanoscience, National Center for Nanoscience and Technology, Chinese Academy of Sciences, Beijing 100190, China; [c]School of Nanoscience and Technology, University of Chinese Academy of Sciences, Beijing 100049, China; [d]Department of Physics, Fudan University, Shanghai 200438, China; [e]College of Chemistry, Key Laboratory of Theoretical and Computational Photochemistry of Ministry of Education, Beijing Normal University, Beijing 100875, China; [f]Department of Materials Science and Engineering, City University of Hong Kong, Kowloon, Hong Kong 999077, China; and [g]Department of Earth and Environmental Science, University of Pennsylvania, Philadelphia, PA 19104

Author contributions: X.C.Z., J.S.F., and Y.G. designed research; D.L., S.W., W.X., Y.C., P.L., X.D., X.Y., and Z.J. performed research; Y.-G.F., W.Z., W.-H.F., X.C.Z., J.S.F., and Y.G. analyzed data; and D.L., S.W., X.C.Z., J.S.F., and Y.G. wrote the paper.

1. D. Tian, Y. Song, L. Jiang, Patterning of controllable surface wettability for printing techniques. *Chem. Soc. Rev.* **42**, 5184–5209 (2013).
2. T. S. Wong *et al.*, Bioinspired self-repairing slippery surfaces with pressure-stable omniphobicity. *Nature* **477**, 443–447 (2011).
3. V. Liimatainen *et al.*, Mapping microscale wetting variations on biological and synthetic water-repellent surfaces. *Nat. Commun.* **8**, 1798 (2017).
4. C. Peng, Z. Chen, M. K. Tiwari, All-organic superhydrophobic coatings with mechanochemical robustness and liquid impalement resistance. *Nat. Mater.* **17**, 355–360 (2018).
5. Y. Gao *et al.*, Turning a superhydrophilic surface weakly hydrophilic: Topological wetting states. *J. Am. Chem. Soc* **142**, 18491–18502 (2020).
6. S. Pan *et al.*, Coatings super-repellent to ultralow surface tension liquids. *Nat. Mater.* **17**, 1040–1047 (2018).
7. A. Tuteja *et al.*, Designing superoleophobic surfaces. *Science* **318**, 1618–1622 (2007).
8. I. U. Vakarelski, N. A. Patankar, J. O. Marston, D. Y. Chan, S. T. Thoroddsen, Stabilization of Leidenfrost vapour layer by textured superhydrophobic surfaces. *Nature* **489**, 274–277 (2012).
9. X. Deng, L. Mammen, H. J. Butt, D. Vollmer, Candle soot as a template for a transparent robust superamphiphobic coating. *Science* **335**, 67–70 (2012).
10. X. Tian, T. Verho, R. H. A. Ras, Moving superhydrophobic surfaces toward real-world applications. *Science* **352**, 142–143 (2016).
11. Z. Yang, J. Wei, Y. I. Sobolev, B. A. Grzybowski, Systems of mechanized and reactive droplets powered by multi-responsive surfactants. *Nature* **553**, 313–318 (2018).
12. E. K. Sackmann, A. L. Fulton, D. J. Beebe, The present and future role of microfluidics in biomedical research. *Nature* **507**, 181–189 (2014).
13. Y. Zeng *et al.*, Miniaturizing chemistry and biology using droplets in open systems. *Nat. Rev. Chem.* **7**, 439–455 (2023).
14. L. Shang, Y. Cheng, Y. Zhao, Emerging droplet microfluidics. *Chem. Rev.* **117**, 7964–8040 (2017).
15. B. E. Debs, R. Utharala, I. V. Balyasnikova, A. D. Griffiths, C. A. Merten, Functional single-cell hybridoma screening using droplet based microfluidics. *Proc. Natl. Acad. Sci. U.S.A.* **109**, 11570–11575 (2012).
16. P. N. Nge, C. I. Rogers, A. T. Woolley, Advances in microfluidic materials, functions, integration, and applications. *Chem. Rev.* **113**, 2550–2583 (2013).
17. A. B. Theberge *et al.*, Microdroplets in microfluidics: An evolving platform for discoveries in chemistry and biology. *Angew. Chem. Int. Ed.* **49**, 5846–5868 (2010).
18. M. Yoshino *et al.*, Engineering surface and development of a new DNA micro array chip. *Wear* **260**, 274–286 (2006).
19. B. K. Park, D. Kim, S. Jeong, J. Moon, J. S. Kim, Direct writing of copper conductive patterns by ink-jet printing. *Thin Solid Films* **515**, 7706–7711 (2007).

20. N. Lorwanishpaisarn *et al.*, Fabrication of durable superhydrophobic epoxy/cashew nut shell liquid based coating containing flower-like zinc oxide for continuous oil/water separation. *Syrf. Coat. Tech.* **366**, 106–113 (2019).
21. Z. Li, H. Zeng, X. Zhang, Growth rates of hydrogen microbubbles in reacting femtoliter droplets. *Langmuir* **38**, 6638–6646 (2022).
22. J. K. Lee *et al.*, Spontaneous generation of hydrogen peroxide from aqueous microdroplets. *Proc. Natl. Acad. Sci. U.S.A.* **116**, 19294–19298 (2019).
23. C. Zhu, J. S. Francisco, Production of hydrogen peroxide enabled by microdroplets. *Proc. Natl. Acad. Sci. U.S.A.* **116**, 19222–19224 (2019).
24. S. Jin *et al.*, The spontaneous electron-mediated redox processes on sprayed water microdroplets. *JACS Au* **3**, 1563–1571 (2023).
25. H. Chen *et al.*, Spontaneous reduction by one electron on water microdroplets facilitates direct carboxylation with CO2. *J. Am. Chem. Soc.* **145**, 2647–2652 (2023).
26. R. N. Wenzel, Resistance of solid surfaces to wetting by water. *Ind. Eng. Chem.* **28**, 988–994 (1936).
27. A. B. D. Cassie, S. Baxter, Wettability of porous surfaces. *Trans. Faraday Soc.* **40**, 546–550 (1944).
28. L. Courbin *et al.*, Imbibition by polygonal spreading on microdecorated surfaces. *Nat. Mater.* **6**, 661–664 (2007).
29. R. Raj, S. Adera, R. Enright, E. N. Wang, High-resolution liquid patterns via three-dimensional droplet shape control. *Nat. Commun.* **5**, 4975 (2014).
30. J. Lou *et al.*, Polygonal non-wetting droplets on microtextured surfaces. *Nat. Commun.* **13**, 2685 (2022).
31. K. H. Chu, R. Xiao, E. N. Wang, Uni-directional liquid spreading on asymmetric nanostructured surfaces. *Nat. Mater.* **9**, 413–417 (2010).
32. C. Ishino, K. Okumura, Wetting transitions on textured hydrophilic surfaces. *Eur. Phys. J. E: Soft Matter. Biol. Phys.* **25**, 415–424 (2008).
33. G. Fang, A. Amirfazli, Understanding the edge effect in wetting: A thermodynamic approach. *Langmuir* **28**, 9421–9430 (2012).
34. K. L. Wilke, Z. Lu, Y. Song, E. N. Wang, Turning traditionally nonwetting surfaces wetting for even ultra-high surface energy liquids. *Proc. Natl. Acad. Sci. U.S.A.* **119**, e2109052119 (2022).
35. R. Seemann, M. Brinkmann, E. J. Kramer, F. F. Lange, R. Lipowsky, Wetting morphologies at microstructured surfaces. *Proc. Natl. Acad. Sci. U.S.A.* **102**, 1848–1852 (2005).
36. T. L. Liu, C.-J.C. Kim, Turning a surface superrepelleteven to completely wetting liquid. *Science* **346**, 1096–1100 (2014).
37. J. W. Gibbs, The Scientific Papers of J. Willard Gibbs. Vol 1: Thermodynamics (Longmans, Green and Co., 1906).
38. J. F. Oliver, C. Huh, S. G. Mason, Resistance to spreading of liquids by sharp edges. *J. Colloid Interface Sci.* **59**, 568–581 (1977).
39. E. Bayramli, S. G. Mason, Liquid spreading: Edge effect for zero contact angle. *J. Colloid Interface Sci.* **66**, 200–202 (1978).
40. D. C. Dyson, Contact line stability at edges: Comments on Gibbs's inequalities. *Phys. Fluids* **31**, 229–232 (1988).
41. V. Liimatainen, V. Sariola, Q. Zhou, Controlling liquid spreading using microfabricated undercut edges. *Adv. Mater.* **25**, 2275–2278 (2013).
42. D. Debuisson, R. Dufour, V. Senez, S. Arscott, Wetting on smooth micropatterned defects. *Appl. Phys. Lett.* **99**, 184101 (2011).
43. K. A. Brakke, The surface evolver. *Exp. Math.* **1**, 141–165 (1992).
44. S. Plimpton, Fast parallel algorithms for short-range molecular dynamics. *J. Comput. Phys.* **117**, 1–19 (1995).
45. V. Molinero, E. B. Moore, Water modeled as an intermediate element between carbon and silicon. *J. Phys. Chem.* **113**, 4008–4016 (2009).